# Photogrammetry Analysis of a Hypersonic Inflatable Aerodynamic Decelerator Structural Test Article

Lin Li[1] and Robert D. Braun[2]
*Georgia Institute of Technology, Atlanta, GA, 30332*

*and*

Alan M. Cassell[3]
*NASA Ames Research Center, Moffett Field, CA*

Analysis was performed on photogrammetry data of a 6m Hypersonic Inflatable Aerodynamic Decelerator (HIAD), an inflatable stacked torus used to aid in atmospheric entry, to understand its structural dynamics. Photogrammetry data was obtained during wind tunnel testing under various loading conditions. Test parameters included the freestream dynamic pressure, yaw angle and internal inflation pressure. In addition, two HIAD configurations were analyzed, the basic stacked torus (Baseline configuration) and a second configuration adding a torus near the shoulder to aid in rigidity (Tri-torus configuration). The analysis includes estimating the deflection of the HIAD under loading as well as calculating the standard deviation relative to the mean deflection and the frequency content of the dynamic response. Under load, the deflection angle for each configuration ranged from 1° to 3° (1σ). The photogrammetry data showed that the oscillatory motion increased with higher dynamic pressure but was insensitive to yaw angle. In addition, the analysis showed that the standard deviation of the HIAD shape with respect to the average deflection increased while moving radially outwards. However, the standard deviation values calculated from different camera pairs were inconsistent as a result of their distances to the test article. The frequency analysis showed that each radial member behaved similarly to a rigid oscillator, having the same frequency content of motion along each radial direction and increased amplitude when moving radially outward. Both the frequency and shape standard deviation analyses showed that the motion of the HIAD was piecewise continuous in the azimuthal direction. These discontinuities are also likely due to the location of different camera pairs. The photogrammetry data is a valuable dataset providing insight into the static and dynamic response of the HIAD under loading. However, inconsistencies in the camera resolution need to be accounted for and higher temporal resolution will improve the fidelity of analysis.

---

[1] Graduate Research Assistant, School of Aerospace Engineering, lli313@gatech.edu
[2] David and Andrew Lewis Professor of Space Technology, School of Aerospace Engineering, robert.braun@aerospace.gatech.edu
[3] Aerospace Engineer, alan.m.cassell@nasa.gov

**Nomenclature**

| | |
|---|---|
| $I$ | Inflation setting |
| $N$ | Number of frames |
| $T$ | Torus |
| $x$ | x-coordinate |
| $y$ | y-coordinate |
| $z$ | z-coordinate |

**Subscripts**

| | |
|---|---|
| $1\text{-}8$ | Tori number (increasing from nose to shoulder) |
| $ave$ | Average over multiple frames |
| $i$ | $i^{th}$ frame |

**Acronyms**

| | |
|---|---|
| EDL | Entry, Descent and Landing |
| DGB | Disk-Gap-Band |
| HIAD | Hypersonic Inflatable Aerodynamic Decelerator |
| IAD | Inflatable Aerodynamic Decelerator |
| IRVE | Inflatable Reentry Vehicle Experiment |
| MSL | Mars Science Laboratory |
| SIAD | Supersonic Inflatable Aerodynamic Decelerator |
| TPS | Thermal Protection System |

## I.   Introduction

One of the most technically challenging aspects of planetary exploration is designing a vehicle that can execute and survive the Entry, Descent and Landing (EDL) phase of the mission. Special care has to be taken so that the entry vehicle can decelerate sufficiently as well as dissipate the large heat load experienced from traveling through the atmosphere during the entry phase.[1] This is typically accomplished using a rigid aeroshell and supersonic parachute system, qualified in the 1960's and 1970's for the Mars Viking mission. Future NASA goals include heavier robotic and eventually human-class missions to other planets, which require larger drag devices to decelerate and safely land the vehicles. This can be achieved either by increasing the diameter of the aeroshell, using a larger parachute, or developing a different EDL system.

Increasing the diameter of the aeroshell is not achievable since they need to first be packaged in the rocket payload shroud, limiting the entry vehicle maximum diameter to 5m.[2] As a result, aeroshells are unable to scale to the size needed to safely land the requisite mass for human Mars exploration. An alternative solution is to increase drag from the aerodynamic decelerator. The most common aerodynamic decelerators have historically been parachute systems.[3] Parachutes have flown on every US manned mission including Apollo, which used both high altitude drogue parachutes for stabilization and main parachutes to achieve a safe terminal velocity.[4-6] However, complications in supersonic parachute inflation and their inability to survive the extreme hypersonic heating conditions place substantial limitations on parachute's abilities to land heavy payloads. As a result, the maximum deliverable payload mass to the Mars surface using a parachute system is estimated to be on the order of a few metric tons (mT). In particular, the recent successful landing of the Mars Science Laboratory (MSL) has already pushed the limit of what is achievable through reliance on incremental advances of the foundational heritage Viking technology.[7] In order to land more massive payloads on Mars and, specifically, to enable future human missions to Mars, a new, innovative technology is required.

One of the proposed EDL technologies is the Hypersonic Inflatable Aerodynamic Decelerator (HIAD). HIADs are of interest for this mission class because such devices inflate to their full size in space and are not directly constrained by the launch vehicle payload shroud diameter as are rigid aeroshells nor inflation conditions like parachutes. They can provide both deceleration and thermal protection capabilities throughout EDL, which would potentially decrease the entry vehicle complexity, providing a more reliable and efficient way to deliver payloads onto the surface of a planet. Another benefit is that HIADs can be deployed either exo-atmospherically or during the hypersonic phase of flight which allows for increased timeline before touch-down, higher landed entry mass or higher landing elevation.

HIAD development was first conducted in parallel with Supersonic Inflatable Aerodynamic Decelerators (SIAD), another type of Inflatable Aerodynamic Decelerator (IAD) that is inflated supersonically[8]. The development of IADs in the United States started as early as the 1960's when Robert W. Lenard from NASA Langley Research Center proposed the inflatable reentry glider for manned reentry from orbital flight[9]. Since then, different IAD configurations have been studied and tested, such as Isotensoids, Stacked Toroids, and Tension Cones both for use as trailing IADs as well as attached IADs[10-19]. One of the most successful and widely used IAD concepts was the Ballute, developed by Goodyear Aerospace Corporation[20]. From the mid 1970's through the mid 1990's, IAD development stagnated since Disk-Gap-Band (DGB) parachutes were fully capable for space missions at the time. Starting in 1995, interest in the development of IADs has been revisited as recently proposed missions to Mars, Titan, and Neptune could not be achieved with the DGB parachute[21]. These missions required a decelerator that could be deployed at either supersonic or hypersonic speeds and is able to bring heavier payloads to the destination planet[22]. However, IAD development has not yet reached the maturity and Technology Readiness Level to be implemented into future space missions. Additional research and developments are required to advance IAD technologies. Several national agencies currently are working on IAD developments including the Air Force[23], DARPA[24], European Space Agency[25], and NASA[26-30]. The most recent HIAD flight tests have been performed at NASA Langley Research Center. The first of these tests was the Inflatable Reentry Vehicle Experiment (IRVE) in September, 2007 however it failed to deploy due to rocket failure. The follow-on mission, IRVE-II, was launched on a Black Brant XI sounding rocket from NASA's Wallops Flight Facility in 2009. IRVE-II employed a 3-meter diameter, 60° half-angle configuration consisting of seven tori, laced together and arranged into three separate inflatable volumes[31]. The article initiated descent supersonically at an altitude of 211 km and the inflatable heat-shield was deployed within 90 seconds at an altitude of 200 km[32]. This flight experiment successfully demonstrated many aspects required of inflatable technologies including exo-atmospheric inflation, inflatable structure performance, flexible thermal protection systems, aerodynamic stability, and structural integrity during atmospheric entry. On July 23rd, 2012, IRVE-III was launched from NASA's Wallops Flight Facility. It had a different configuration than IRVE-II but same diameter. This project further demonstrated the potential capability of the HIAD technology including the use of a center of gravity offset to generate lift as well as providing higher peak heating to test the flexible Thermal Protection System (TPS) capabilities.



**Figure 1. Cross-sectional view of the HIAD structure**

In order for HIADs to be considered for future missions there must be confidence in their ability to perform successfully as an entry device in the conditions in which they will be flown. Given that limitations of ground-test facilities prevent full scale testing, this entails ensuring that they perform successfully during wind tunnel and flight-testing and that those test results can be correlated to relevant flight regimes to predict their capabilities under those environments. Analyzing such test data for stability and drag performance allows for characterization of HIAD performance as a drag device under the flight relevant conditions. In addition, transferring this data to flight regimes outside of those being tested requires confidence in the models being used to describe the HIAD and the ability of these models to capture the relevant physics both within and outside the test conditions. This investigation focuses on estimating the inflated shape and dynamics of a 6m 60-degree half-angle sphere cone HIAD test article under a range of loading conditions.

## II. Ground Test Campaign

The HIAD configuration is composed of two major components: a rigid center-body made of Aluminum and several tori composed of fiber reinforced thin films. Kevlar straps hold the tori together. In addition, the HIAD investigated has an aerodynamic skin cover that mimics the structure of a flexible TPS.[33] Two configurations were tested, seen in Fig. 1. The Baseline configuration is composed of seven structural tori ($T_1$-$T_7$) and one shoulder torus ($T_8$). The second configuration, called the Tri-torus, builds upon the Baseline configuration by adding an additional torus located between $T_6$ and $T_7$ ($T_{6.5}$) (also seen in Fig. 1 in the bright red circle) and was developed to investigate whether this addition substantially improved rigidity.
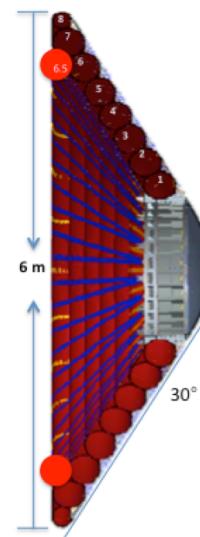
Testing of the 6m diameter HIAD was conducted in the 40 by 80 foot wind tunnel at NASA Ames Research Center with the HIAD mounted on a sting. In the wind tunnel, four pairs of stereoscopic camera systems were mounted in the center, lower, and upper sections of the East wall as well as on the floor and ceiling.[33] The set-up was chosen to provide a full view of the HIAD and to permit 3D tracking. This is shown in Fig. 2. Each camera acquired data at 15 Hz for 10 seconds producing 150 frames for each dataset and was synched by a signal pulse



**Figure 2. Photogrammetry camera setup**[35]

from the facility data acquisition system. Camera placement was determined before testing by using virtual imaging software in order to meet the design and resource constraints in the wind tunnel environment.[34] Photogrammetry software (ARAMIS®) was used to generate the full 3D model and the photogrammetry data obtained from each camera pair was stitched together with SVIEW®.

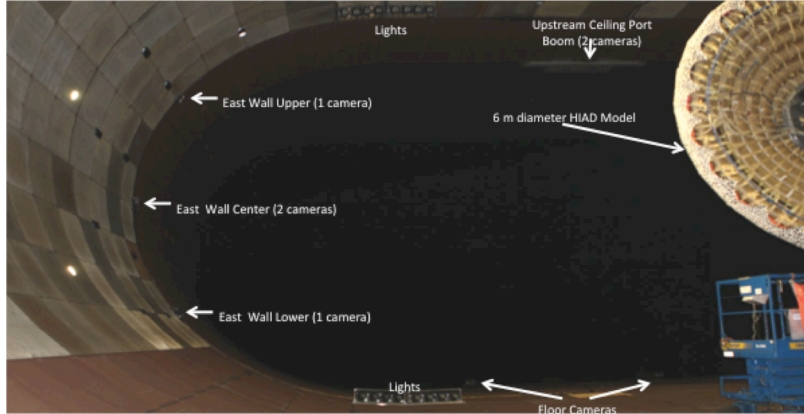In order to develop a deflection data set sufficient to validate aero-elastic models, three parameters were studied: yaw angle, free-stream dynamic pressure, and inflation pressure. The test matrix can be seen in Table 1.

**Table 1. Test matrix**

| Yaw Angle (deg) | Dynamic Pressure (psf) | Inflation Pressure (psi) | |
|---|---|---|---|
| -25, -15, -5, 0, 5, 10 | 8, 40, 50, 65, 70 | $I_2$ | 15 (all tori) |
| | | $I_3$ | 10 ($T_{3-6,8}$), 15 ($T_{1,2,7}$) |
| | | $I_4$ | 8 ($T_{3-6}$), 15 ($T_{1,2,7}$) |

The yaw angle was modulated to simulate an angle of attack during actual flight. Positive yaw angles were defined as a clockwise rotation when looking down upon the wind tunnel. Dynamic pressure was changed by adjusting the freestream air velocity. The maximum wind tunnel dynamic pressure was limited to 70 psf by NFAC safe operating procedures. The last parameter analyzed was the inflation pressure of the individual tori. Three settings were used to investigate the sensitivity of the HIAD stiffness to inflation pressure.[33]

## III.   Methodology and Results

### A.  Photogrammetry Data Uniqueness

The photogrammetry measurements are used to determine the aeroshell shape and deformation under the range of test parameters.[31] A full 3D HIAD model was constructed by combining data obtained from at least two camera-pairs. Figure 3a shows an example of the data captured by the four different stereoscopic camera-pairs during a run. The data in this figure is represented by colors while gray is an area of no information. When multiple views are
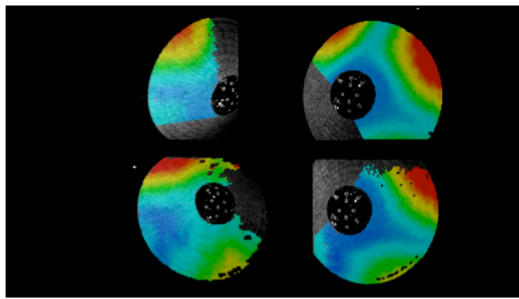


(a) Images from separate camera pairs taken from ARAMIS
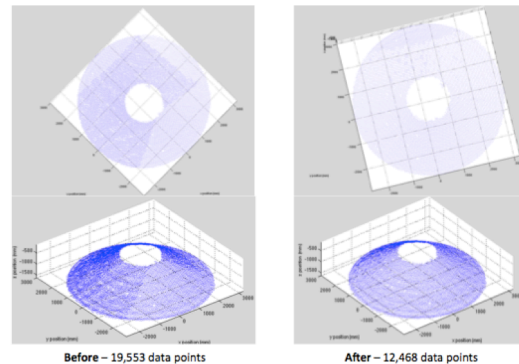


(b) HIAD model before and after data cleanup

**Figure 3. Photogrammetry stitching and data cleanup**

stitched together to create the full model, overlapping sections contain redundant information increasing the computational cost when performing data analysis. A MATLAB® script was written to delete the overlapping data. A comparison of data files before and after running the MATLAB script showed that the resulting files were approximately 60% of their original size. Depiction of the photogrammetry data before and after the clean-up can be seen in Fig. 3b.

### B. Deflection Angle Measurements

One use of the photogrammetry data was to have quick feedback of the HIAD behavior in a wind tunnel environment before performing higher fidelity analysis. For consistency, the deflection angle was calculated based on the location of the peaks of tori $T_1$ and $T_7$. Given the symmetry of the problem, it was of interest to calculate the deflection angle at four radial directions: 0° (up, N), 90° (right, E), 180° (down, S), and 270° (left, W). (The yaw plane is aligned with the 90° and 270° directions). Much like exporting the full 3D HIAD model from the photogrammetry software, the data along the peaks of $T_1$ and $T_7$ could also be exported individually. This was done by selecting three points on the desired peak, which would generate a circle of data that could be exported. This process is shown in Fig. 4a.

A MATLAB routine was developed to compute the deflection angles. The code finds the points on tori $T_1$ and $T_7$ corresponding to the 0°, 90°, 180°, and 270° radial directions. These points were used to create vectors and the resulting vectors were used to calculate the overall deflected angle of the HIAD in each direction. This process can be seen in Fig. 4b. These angles could then be compared to the no wind case and the difference used to infer the loaded



(a) Exporting $T_1$ and $T_7$ from the photogrammetry software



(b) Vectors used to calculate the deflected angle

**Figure 4. Visualization of deflected angle calculations**

deformation. Note in Fig. 4b that the sides of the HIAD form a concave shape, in this instance more pronounced on the 270° radial direction. This analysis does not recover the shape of the deformation or any resulting effects, but instead provides a first order approximation of the deflected cone angle. Other analyses try to account for this phenomenon by performing a line fit of all points along a given radial direction.[35]

An overall comparison was performed that looked at the deflection of the Baseline and Tri-torus configurations over all available data sets. In this way, average performance of both configurations could be assessed. The deflection angles for the Baseline and Tri-torus configurations under all available test conditions and for each radial direction (0°, 90°, 180° and 270°) are plotted together in Fig. 5. It can be seen that both the Baseline and Tri-torus configurations have deflection angles between 0° and 5°. However, the Baseline configuration has one point that had a deflection angle of around 8.5°, seen in Fig. 5a. Since there are no other deflection angles near this value (even when considering the other radial direction of that same run) it was decided that this point was an outlier, likely due to the inaccuracy of determining the peak of $T_1$ and $T_7$ or due to rapid oscillations for that case. Therefore, it was discarded in Fig. 5b.

Table 2 displays the deflection angle statistics for data shown in Fig. 5 for both the Baseline and Tri-torus configurations. When looking at the average of all cases it can be seen that the Baseline and Tri-torus configuration have, on average, a deflected angle of 2°. When accounting for the standard deviation in these results, the deflection angles of the Baseline and Tri-torus are each in the range of 1° to 3°. As evidenced by Fig. 5b, the tri-torus configuration does not exhibit an overall decrease in deformation at $T_7$, or decrease the deformation of the overall cone angle, over the course of the test program. However, the static load test program concluded that the tri-torus was more rigid than the baseline configuration.[36] In addition, differences in the HIAD shape between the two configurations could affect the drag, stability and heating of the HIAD, which is not accounted for in this analysis.
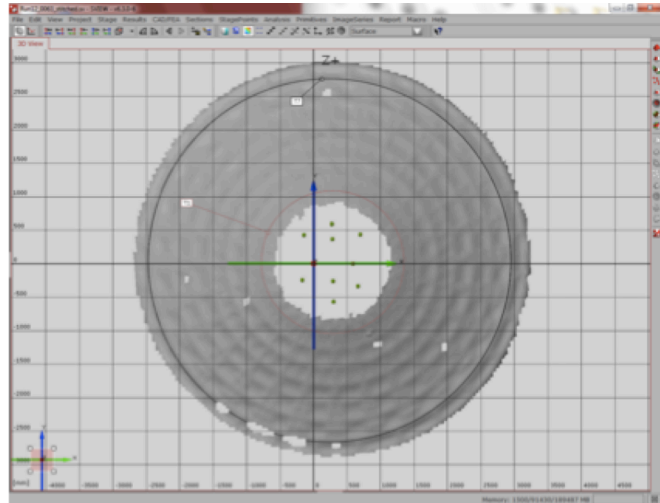
(a) All deflected angle results          (b) All deflected angle results (without outlier point)
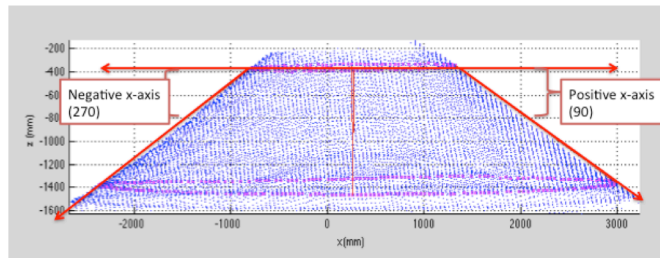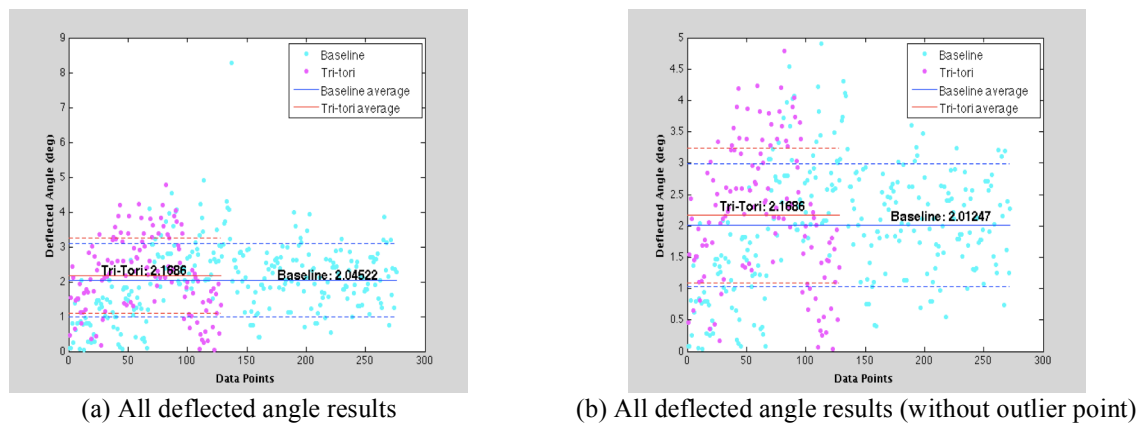
**Figure 5. All deflected angle results with statistics**

**Table 2. Summary of all deflected angle results**

|  | Baseline | Tri-torus | % Difference (compared to baseline) |
|---|---|---|---|
| Average Deflection | 2.01° | 2.17° | 7.80% |
| Standard Deviation | 0.98° | 1.08° | 10.20% |
| Max Deflection | 4.91° | 4.79° | -2.44% |
| Median Deflection | 2.02° | 2.15° | 6.44% |

The uncertainty of the calculations presented here are unknown at this time since the error in the cameras, calibration, and imaging are not included. Other analyses observed qualitative hysteresis effects from rotating the HIAD through a range of yaw angles.[35] Since this data was collected over the entire test program, these effects could potentially mask differences between the baseline and tri-torus configurations. For a better understanding of the Baseline and Tri-torus performance, error bars can be included to understand the certainty of the results. The error bars for both configurations are assumed to be the same since the same photogrammetry system was used for each. For this first order analysis, the standard deviation values were provided to indicate the variation across all trials.

## C.  Averaging Routine

There were large errors between deflection angles calculated from different frames of photogrammetry data due to the HIAD oscillations during testing. These errors clouded trends in the data and motivated the use of a single data set that was representative of all 150 frames. Thus, a MATLAB script was created to average the data points among all of the frames. When the photogrammetry software outputs the 3D coordinates of a point on the HIAD surface it also provides a unique set of indices for that point that can identify it in each frame of data. An example of point coordinates and indices can be seen in Fig. 6. The MATLAB script first saves all of the points to a file and sorts them by their indices, grouping points with like identity indices. It then iterates through each set of identity indices and averages the resulting set of 3D positions to produce an averaged position. The average is calculated using equation 1 taking into account the total number of frames that contain the given point.

| Point Indices | | | Point Coordinates | | |
|---|---|---|---|---|---|
| x-index | y-index | Sub-index | x | y | z |
| 135 | 22 | 0 | 142.25 | 3006.74 | -1443.57 |
| 136 | 22 | 0 | 187.44 | 3004.81 | -1430.71 |
| 137 | 22 | 0 | 235.38 | 3002.06 | -1420.90 |
| 138 | 22 | 0 | 285.21 | 2999.04 | -1413.27 |
| 139 | 22 | 0 | 335.71 | 2995.60 | -1406.32 |
| 140 | 22 | 0 | 388.40 | 2991.61 | -1401.47 |
| 141 | 22 | 0 | 441.31 | 2987.70 | -1396.74 |
| 142 | 22 | 0 | 495.35 | 2983.67 | -1393.02 |

**Figure 6. 3D position of photogrammetry points including the identity matrix**

$$x_{ave} = \frac{1}{N}\sum_{i=1}^{n}x_i \; ; \; y_{ave} = \frac{1}{N}\sum_{i=1}^{n}y_i \; ; \; z_{ave} = \frac{1}{N}\sum_{i=1}^{n}z_i \quad\quad (1)$$

In cases where the photogrammetry does not identify a point in one or more frames, these frames do not contribute to that point's averaged position since the MATLAB routine cannot find the point's identifier. The script stores the averaged position of every point as the averaged data set and outputs the data to a file for use in future analysis.

## D. Standard Deviation to Estimate HIAD Oscillations

It was shown that oscillation of the HIAD caused significant deviations between different frames of a single test run. To quantify the average response of the HIAD as well as estimate the oscillatory motion, the standard deviation in position among all 150 frames of a single run was calculated. Regions of high standard deviation indicate significant motion while regions of low standard deviation indicate limited motion. In addition, localized regions of high standard deviation may indicate a structural defect or other phenomena. The standard deviation of each point about its mean location was calculated via Eq. 2.

$$\sigma_x = \sqrt{\frac{1}{N}\sum_{i=1}^{N}(x_i - x_{ave})^2} \; ; \; \sigma_y = \sqrt{\frac{1}{N}\sum_{i=1}^{N}(y_i - y_{ave})^2} \; ; \; \sigma_z = \sqrt{\frac{1}{N}\sum_{i=1}^{N}(z_i - z_{ave})^2} \quad (2)$$



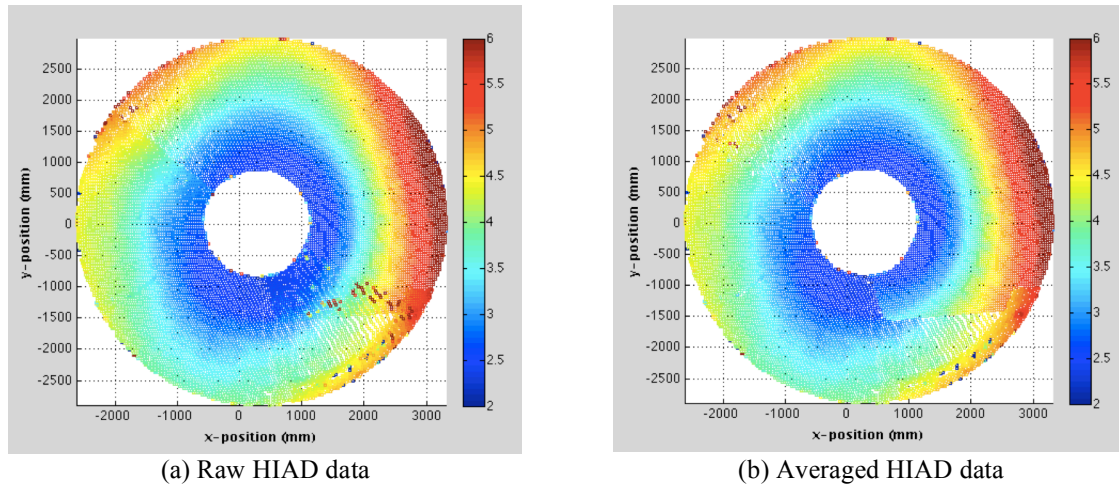(a) Raw HIAD data         (b) Averaged HIAD data

**Figure 7. Standard deviation in the absolute position of all points on the HIAD (70 psf, -25$^o$ yaw angle, $I_3$ inflation setting)**

Figure 7 shows a top down view the HIAD depicting the standard deviation in the absolute position of each point. This run was performed at 70 psf with a -25$^o$ yaw angle and $I_3$ inflation setting. Two observations can be made from the graphs. The first observation is that there is a small cluster of high deviation points along the 135$^o$ radial direction (southeast direction) in Fig. 7a. Since these points are on the interface of the two different camera pairs, they are likely artifacts created from stitching together the different views and do not have physical significance. The points were removed after running the MATLAB data clean-up script.

The second observation is that the standard deviation in position increases when moving radially outward from the center but is not radially uniform across the entire HIAD. If the HIAD were a rigid oscillator, the points on the perimeter would have more motion than points near the center and would thus have a higher standard deviation in their position. This is apparent in Fig. 7. However, the standard deviation would be symmetric about the *y*-axis with highest standard deviation occurring along the yaw plane ( $y = 0$ ). In this case, there is a distinct difference between the lower left and upper right portions of the graph. In particular, across the interface of the two data sets (along the 135$^o$ and 315$^o$ radial directions) a noticeable change in positional standard deviation can be seen. These two regions correspond to imaging of the HIAD from different camera pairs. The fact that they do not observe the same deviation at their interface could potentially be caused by differing resolutions of each camera pair. All cameras used for photogrammetry had the same sensor and lens setup. Therefore, differences in resolution are a function of distance from the camera to the test article. Since the cameras imaging the top-right portion of the HIAD were the

closest for this run, they have the highest resolution and thus minimize the error due to uncertain tracking of the HIAD surface.

This phenomenon is also seen in a different run, tested at 40 psf with a $0^o$ yaw angle and $I_3$ inflation setting. As seen in Fig. 8, the standard deviation in position observed from the wall camera pair is much lower than that observed from the bottom pair. When the two views are stitched together (shown in Fig. 8c), the datasets are simply overlaid. Figure 8b shows a higher positional standard deviation compared to Fig. 8a for points in the same location. This discrepancy matches the hypothesis that the floor camera pair yields a lower resolution relative to the wall pair due to their further distance from the test article. The standard deviation in Fig. 8a varies radially while that of Fig. 8b varies with radius and y-position. The wall camera pair was mounted at the same height as the HIAD so resolution is a weak function of y-position. However, the floor cameras were located below the HIAD. Therefore, their resolution was highly dependent on the y-position of the tracked points. In this case, the data from the top camera pair has less uncertainty and is expected to portray a more representative measure of the HIAD oscillation. For a more accurate assessment, the positional uncertainty due to the camera sensing should be evaluated for each point to understand the uncertainty in the standard deviation measurements presented.
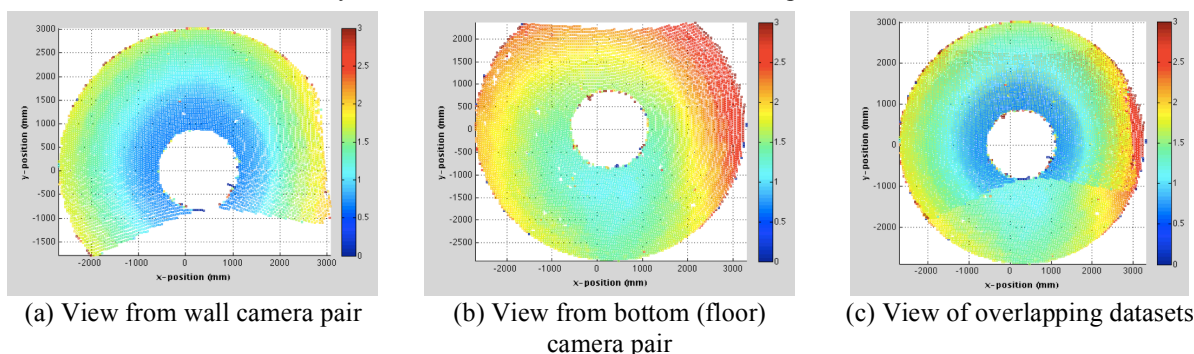


(a) View from wall camera pair    (b) View from bottom (floor) camera pair    (c) View of overlapping datasets

**Figure 8. Standard deviation of HIAD photogrammetry data including views from each individual camera**

It is also important to investigate how sensitive the positional standard deviation of each point is to the different test parameters. Figure 9a shows the standard deviation results for two runs conducted at different dynamic pressures while Fig. 9b shows the results from two runs conducted with different yaw angles. These graphs illustrate the overall standard deviation for a particular set of test conditions. The shape of each graph is not important since the points are plotted without regards to their order nor is the number of points important since it is dependent on the number and viewing angles of the camera pairs, neither of which are important to this discussion. Figure 9a shows that positional standard deviation increases with increasing dynamic pressure. This indicates that there is more HIAD motion with increased flow velocity, which makes physical sense. This was also observed qualitatively during testing. Figure 9b indicates that there is no substantial change in the overall positional standard deviation with varying yaw angle. This also makes physical sense. While motion would likely increase on the side normal to the flow, this would likely be counteracted by reduce motion on the other side.
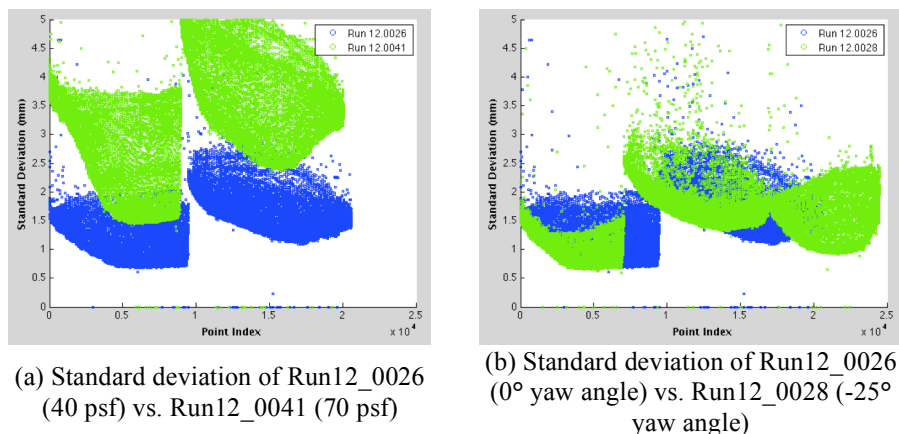


(a) Standard deviation of Run12_0026 (40 psf) vs. Run12_0041 (70 psf)

(b) Standard deviation of Run12_0026 (0° yaw angle) vs. Run12_0028 (-25° yaw angle)

**Figure 9. Standard deviation comparisons between different dynamic pressures and yaw angles**

It is important to note the potential sources of uncertainty in this analysis. As discussed above, different camera pairs have different resolution based on their distance to the HIAD. This is not expected to affect the results of Fig.

9a since the cameras were the same distance for both runs, but it could potentially affect the uncertainty of the data in Fig. 9b since the HIAD model was rotated. In this case, imaging from the floor cameras would produce higher overall uncertainty and imaging from the wall cameras would produce lower uncertainty but its affect on Fig. 9b is uncertain since the location of each data point is not retained. Hysteresis effects could also distort the results since differences in loading fatigue over the course of the test program and on different sides of the HIAD could potentially influence its motion.

### E. Oscillation Frequency to Predict External Forcing

There is significant interest in describing the oscillations that were observed during testing to understand the HIAD dynamics and infer its stability. Given that the HIAD is a blunt body it was hypothesized that oscillations would result from vortex shedding, estimated to be 2-3 Hz.[35] Thus the frequency of oscillation was investigated in order to determine if low frequency content could be detected with this experimental set-up and if it could be correlated to vortex shedding or another known source.

A frequency analysis was performed on a single point using its position data over time. For each run, 4 points were chosen along each of the 0°, 90°, 180° and 270° radial directions. The locations of these points are shown in Fig. 10a as red dots. In this way, motion at different frequencies could be isolated and analyzed to see if there were trends with inflation setting, yaw angle or free-stream dynamic pressure. For each point, a Discrete Fast Fourier Transform was taken of its position over the 150 frames (over time) to determine the frequency content of its motion. Frequencies with the highest amplitudes corresponded to the dominant modes of motion. Figures 10b and 10c show the time signal and FFT for the points along the 90° and 270° radial directions for a run with an $I_3$ inflation setting, dynamic pressure of 70 psf and -25° yaw angle (yaw towards the 270° radial direction).
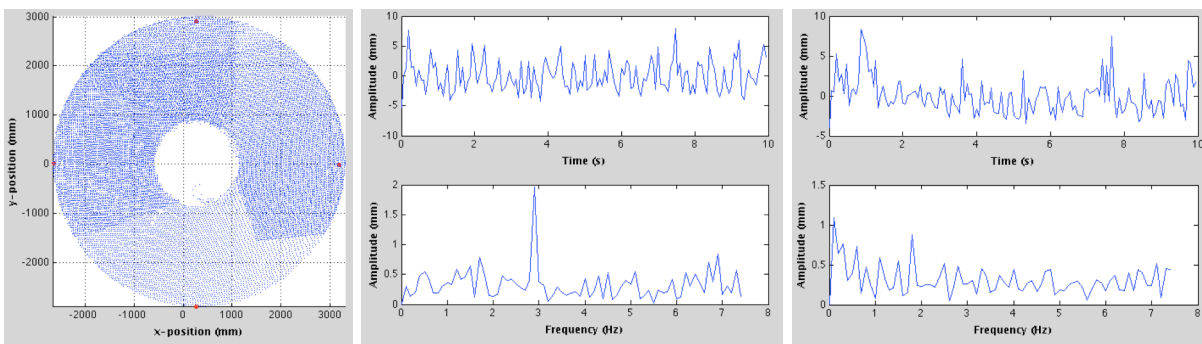


(a) Points chosen for FFT

(b) Signal and FFT for total motion of a single point in 90° radial direction

(c) Signal and FFT for total motion of a single point in 270° radial direction

**Figure 10. Motion in the time and frequency domains for select points on the HIAD**

It is necessary to perform an FFT of the amplitude vs. time graphs (top of Figs. 10b and 10c) to determine frequency content since the motion is chaotic. However, even the FFT graphs do not show a clear overall trend. An ideal FFT would show spikes at a few dominant forcing frequencies with zero amplitude signals everywhere else. Since noise is always present, it would show in the FFT graph as a band of low but relatively constant amplitude data spanning the entire frequency range. Figure 10b shows a promising graph with a very high amplitude peak at 2.9 Hz and moderately low noise surrounding it. However, when looking at Fig. 10c, no dominant peak is seen at all.

The photogrammetry cameras sampled data at 15 Hz. In order for a Discreet Fourier Transform to avoid aliasing of a signal the sampling frequency must be at least 2 times the highest frequency of that signal.[37,38] It is uncertain whether or not 15 Hz was large enough to meet this criterion since the highest frequency of oscillation is not known. Therefore, while the method has promise, it should be applied to other data sources with higher sampling rates to see if it can resolve the dominant forcing frequencies. In addition, the data points were sampled with multiple camera pairs having different resolutions due to their locations. This could potentially decrease the signal to noise ratio and obscure any forcing frequencies. Hysteresis effects could also have an effect since the HIAD did not experience symmetric loading throughout the test campaign. While it is unclear whether this would obscure the dominant forcing frequencies in the FFT plot or simply shift or distort them, this should also be investigated using data with a higher sampling frequency. Finally, wake effects and interaction with the sting could distort or obscure the data. Given that the HIAD was set at a large yaw angle, these effects would be manifested differently along different radial directions.

## F. Oscillation Frequency to Analyze HIAD Motion

Even though the FFT method did not resolve specific forcing frequencies it still provides insight into the HIAD oscillations. Two analyses were performed to estimate the rigidity of the HIAD: 1. along a single radial direction and 2. azimuthally along a constant radius circle. Rigidity was determined based on all points moving cohesively, evidenced by them each having the same frequency content of motion.

The rigidity of the HIAD along each radial direction was investigated by taking the FFT of the position history for multiple points along a single radial direction (both on the peaks of each torus as well as in between tori). Figure 11 shows the FFT results along the $0^o$ radial direction ($+y$ direction) for a run conducted at 70 psf, yaw angle of $0^o$ and $I_3$ inflation setting. Figure 11a plots the distance away from the nose versus the frequency content of motion. Marker size and color is determined by the amplitude of the signal at that frequency (as determined by the FFT). A distinct high frequency peak at around 3 Hz is found in each plot and smaller peaks are also observed. All peaks in the FFT graphs align and all graphs are the same shape (seen in the vertical lines spanning Fig. 11a). This shows that each point along the radial direction acts cohesively and oscillates at the same frequency. Figure 11b also depicts the oscillation frequency versus distance away from the nose ($x$ and $y$-axes, respectively), and includes the amplitude of motion at each frequency on the $z$-axis. The peak frequencies at each distance away from the nose all align. Furthermore, the amplitude increases while moving outwards from the nose cone so points on the outer tori have greater displacement than points on inner tori. As a result, movement along a single radial direction behaves like a rigid rod constrained by the aluminum nose cone.
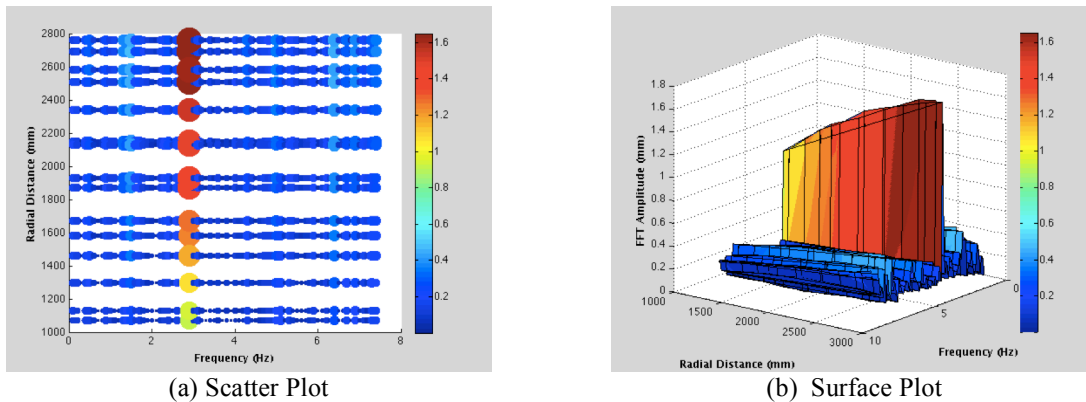


(a) Scatter Plot



(b) Surface Plot

**Figure 11. Frequency content of motion along the $0^o$ radial direction (70 psf, -25$^o$ yaw angle, $I_3$ inflation setting)**



(a) Location of Points Chosen for Analysis
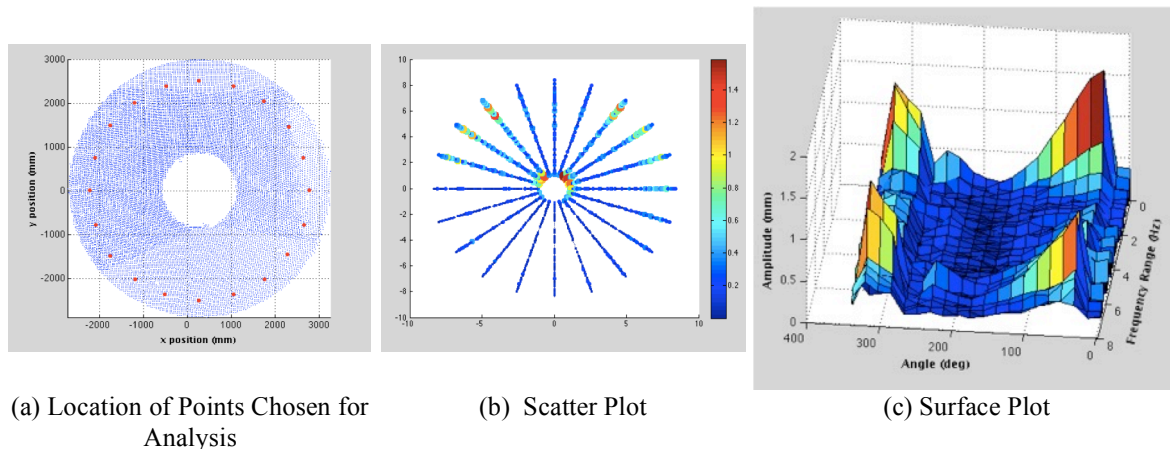


(b) Scatter Plot



(c) Surface Plot

**Figure 12. Frequency content of motion when traveling azimuthally, 2.5m from the HIAD nose (70 psf, $0^o$ yaw angle, $I_3$ inflation setting)**

The rigidity of the HIAD along azimuthal directions was investigated by selecting 20 points distributed uniformly, all 2.5m away from the center (seen in Fig. 12a). Diagrams are shown for a run conducted at 70 psf, $0^o$ yaw angle and $I_3$ inflation setting. The scatter plot depicts the frequency content of motion for each radial direction plotted in a polar graph with low frequencies towards the center and higher frequencies found radially outward (Fig. 12b). Higher amplitude signals are shown via colors and larger markers. The surface plot also shows frequency

content of motion versus azimuthal angle (*x* and *y*-axes, respectively) and includes signal amplitude on the *z*-axis (Fig. 12c).

The surface plot shows a continuous valley between $35^o$ and $250^o$, which is to be expected if the HIAD were a rigid cone oscillating about the pitch plane. There are also large, discontinuous jumps in oscillation amplitude at $20^o$, $280^o$ and $340^o$ showing that the HIAD is not rigid at these locations. However, discontinuous motion was not observed during wind tunnel testing so this analysis was expected to produce a continuous frequency graph. When comparing Figs. 12a and 12b, the locations of the discontinuities match with where the camera pair views overlap (denoted by intensity of color in Fig. 12a). Therefore, the FFT graphs are continuous for individual camera pairs, but discontinuous in overlapping regions. This was the same result seen from the standard deviation analysis and again highlights differences in resolution of the different camera pairs.

## IV.    Summary

Many avenues have been explored to analyze HIAD static and dynamic characteristics while under different loading conditions, including deflection angle measurements as well as calculating the standard deviation of the deformed shape and frequency response quantification. The deflection angle results show that the deflection of the $T_7$ torus of the tri-torus configuration was similar to the baseline configuration over all of the tests performed. Calculations of the standard deviation about the mean deflection show that motion of the HIAD increases while moving radially outwards and that motion was significantly higher in the yaw plane. It was seen that the overall standard deviation increases with increasing dynamic pressure, but is relatively constant with yaw angle. Observing the positional standard deviation of the points along the entire HIAD showed that the locations of the different camera pairs caused significant differences in their standard deviation estimates in overlapping regions. The frequency analysis showed that high frame-rate photogrammetry is necessary to predict external forcing on the HIAD to avoid aliasing of higher frequency signals. Frequency analysis also showed that the frequency content of motion was continuous along a single radial direction. The amplitude of motion increases when moving radially outward showing that each radial direction behaves similar to a rigid rod constrained at one end by the center-body. In addition, the frequency content of motion was continuous azimuthally for each camera pair. However, as with the positional standard deviation analysis, the dataset was discontinuous at the interface of different camera pairs likely due to their locations.

While many observations have been made on the HIAD dynamics, improvements to the photogrammetry setup will allow future test programs to take full advantage of the analyses. For these data reduction techniques it is important that all of the photogrammetry cameras have similar resolution of the test article. This avoids discontinuities at their interface of different camera pairs and provides a consistent description of motion at all points on the test article. Therefore, camera pairs should either be located equal distances from the target or have a resolution that is much smaller than the predicted oscillations. In addition, for a reliable analysis of the frequency response, the frame rate of the cameras should be greater than twice the frequency of the highest expected signal.

## V.    Acknowledgments

## VI.    References

[1] Braun, R. D. and Manning, R. M., "Mars Exploration Entry, Descent, and Landing Challenges," *Journal of Spacecraft and Rockets*, Vol. 44, No. 2, 2007, pp. 310 –323.

[2] Atlas V Launch Services User's Guide". Centennial, CO: United Launch Alliance. 2010-03. Retrieved 2011-12-04.

[3] Gold, D., "Early Development of the Manually Operated Personnel Parachute, 1900-1919," Proceedings of the DOD/AIAA Aerodynamic Deceleration Systems Conference, edited by E. C. Myers, Air Force Flight Test Center, Edwards Air Force Base, Calif., FTC-TR-69-11, Vol. II, April 1969, pp. 403-416.

[4] Hillje, Ernest R., "Entry Aerodynamics at Lunar Return Conditions Obtained from the Flight of Apollo 4 (AS-501)," NASA TN D-5399, (1969)

[5] Knacke, T. W., "The Apollo Parachute Landing System," Proceedings of the DOD/AIAA Aerodynamic Deceleration Systems Conference, edited by E. C. Myers, Air Force Flight Test Center, Edwards Air Force Base, Calif., FTC-TR-69-11, Vol. II, April 1969, pp. 329-338.

[6] Kiker, J. W., "The Apollo Recovery System," presented at Deutsche Gesellschaft fur Luft-und Raumfahrt E. V., Deutsche Forschungs-und Versuchsanstalt, and Advisory Group for Aerospace Research and Development

Symposium on Aerodynamic Deceleration, Technical University of Braunschweig, West Germany, Sept. 15-19, 1969

[7] Way, D. W., et al, "Mars Science Laboratory: Entry, Descent, and Landing System Performance," IEEE Aerospace Conference, Big Sky, MT, March 3-10, 2006.

[8] Cruz, J.R., Lingard, J.S., "Aerodynamic Decelerators for Planetary Exploration: Past, Present, and Future," AIAA Guidance, Navigation, and Control Conference and Exhibit, AIAA 2006-6792, August 2006.

[9] Leonard, R.W., Brooks, G.W., McComb Jr., H.G., "Structural Considerations of Inflatable Reentry Vehicles," NASA Technical Note, NASA TN-D-457, September 1960.

[10] Charczenko, N., McSheara, J.T., "Aerodynamic Characteristics of Towed Cones Used as Decelerators at Mach numbers from 1.57 to 4.65," NASA Technical Note, NASA TN-D-994, December 1961.

[11] Alexander, W.C., "Investigation to Determine the Feasibility of Using Inflatable Balloon Type Drag Devices for Recovery Applications in the Transonic, Supersonic, and Hypersonic Flight Regime Part II: Mach 4 to Mach 10 Feasibility Investigation," Flight Accessories Laboratory Technical Report, ASD TDR 62-702, December 1962.

[12] Charczenko, N., "Aerodynamic Characteristics of Towed Spheres, Conical Rings, and Cones Used as Decelerators at Mach Numbers from 1.57 to 4.65, NASA Technical Note, NASA TN-D-1789, April 1963.

[13] Deitering, J.S., Hilliard, E.E., "Wind Tunnel Investigation of Flexible Aerodynamic Decelerator Characteristics at Mach Numbers 1.5 to 6.0," ARO Inc. Technical Report, AEDC TDR-65-110, June 1965.

[14] Kyser, A.C., "Deployment Mechanics for an Inflatable Tension-Cone Decelerator," NASA Contractor Report, NASA CR-929, November 1967.

[15] Reichenau, D.E.A., "Investigation of an Attached Inflatable Decelerator System for Drag Augmentation of the Voyager Entry Capsule at Supersonic Speeds," ARO Inc. Technical Report, AEDC TR-68-71, April 1968.

[16] Baker, D.C., "Investigation of an Inflatable Decelerator Attached to a 120-deg Conical Entry Capsule at Mach Numbers from 2.55 to 4.40," ARO Inc. Technical Report, AEDC TR-68-227, October 1968.

[17] Bohon, H.L., Miserentino, R., "Attached Inflatable Decelerator (AID) Performance Evaluation and Mission-Application Study," Journal of Spacecraft, Vol. 8, No. 9, September 1971.

[18] Creel, T.R., Miserentino, R., "Aerodynamic Heating at Mach 8 of Attached Inflatable Decelerator Configurations," NASA Technical Memorandum, NASA TM-X-2355, October 1971.

[19] Willis, C.M., Mikulas Jr., M.M., "Static Structural Tests of a 1.5-Meter-Diameter Fabric Attached Inflatable Decelerator," NASA Technical Note, NASA TN-D-6929, October 1972.

[20] Nebiker, F.R., "Development of a Ballute Recovery System for Mach 10 Flight and Its Practical Applications," Goodyear Aerospace Corporation Contractor Report, GER-11467A, August 1964.

[21] Fallon II, E.J., "Supersonic Stabilization and Deceleration: Ballutes Revisited," AIAA 95-1584-CP, 1995.

[22] Cianciolo, A. D., et al, "Overview Of The NASA Entry, Descent and Landing Systems Analysis Exploration Feed-Forward Study," International Planetary Probe Workshop, 2011.

[23] Graham, W.A., "MK 82 Ballute Retarder System Updated for Advanced Weapons Program," 16th Aerodynamic Decelerator Systems Technology Conference and Seminar, AIAA 2001-2039, May 2001.

[24] Iannotta, B. "Future Mars Craft Inspires High-Tech Spy Plane," Space.com Online Publication, Posted 31 October 2007.

[25] Walther, S. et al., "New Space Application Opportunities based on the Inflatable Reentry & Descent Technology (IRDT)," AIAA/ICAS International Air and Space Symposium and Exposition: The Next 100 Years, AIAA 2003-2839, July 2003.

[26] Miller, K.L., Gulick, D., Lewis, J., Trochman, B., Stein, J., Lyons, D.T., Wilmoth, R.G., "Trailing Ballute Aerocapture: Concept and Feasibility Assessment," 39th AIAA/ASME/SAE/ASEE Joint Propulsion Conference and Exhibit, AIAA 2003-4655.

[27] Hughes, S.J., Dillman, R.A., Starr, B.R., Stephan, R.A., Lindell, M.C., Player, C.J., Cheatwood, F.M., "Inflatable Re-entry Vehicle Experiment (IRVE) Design Overview," 18th AIAA Aerodynamic Decelerator Systems Technology Conference and Seminar, AIAA 2005-1636, September 2005.

[28] Richardson, E.H., Munk, M.M., James, B.F., Moon, S.A., "Review of NASA In-Space Propulsion Technology Program Inflatable Decelerator Investments," 18th AIAA Aerodynamic Decelerator Systems Technology Conference and Seminar, AIAA 2005-1603, July 2005.

[29] Masciarelli, J.P., Lin, J.K.H., Ware, J.S., Rohrschneider, R.R., Braun, R.D., Bartels, R.E., Moses, R.W., Hall, J.L., "Ultra Lightweight Ballutes for Return to Earth from the Moon," 47th AIAA/ASME/ASCE/AHS/ASC Structures, Structural Dynamics, and Materials Conference, AIAA 2006-1698, May 2006.

[30] Player, C., "Inflatable Aerodynamic Decelerators Technology Development," Fundamental Aeronautics 2007 Annual Meeting Conference Proceedings, October 2007.

[31] Lindell, M. C., Hughes, S. J., Dixon, M., and Willey, C. E. (2006). "Structural Analysis and Testing of the

Inflatable Re-entry Vehicle Experiment (IRVE)," AIAA Paper AIAA 2006-1699, 47th AIAA/ASCE/AHS/ASC Structures, Structural Dynamics, and Materials Conference, Newport, RI, May 1-4, 2006.

[32] NASA Launches New Technology: An Inflatable Heat Shield, NASA Mission News, 2009-08-17, accessed 2011-01-02.

[33] Cassell, A.M., Swanson, G.T., Johnson, R.K., Hughes, S.J., and Cheatwood, F.M.. "Overview of the Hypersonic Inflatable Aerodynamic Decelerator Large Article Ground Test Campaign," 21st AIAA Aerodynamic Decelerator Systems Technology Conference and Seminar, May, 2011.

[34] Kushner, L.K., Schairer, E.T., "Planning Image-Based Measurements in Wind Tunnels by Virtual Imaging," 49th AIAA Aerospace Sciences Meeting, AIAA 2011-930, Orlando, FL.

[35] Kazemba, C. D., Cassell, A. M., Kushner, L. K., Tran, K., Quach, B. T., Li, L., et. al., "Determination of the Deformed Structural Shape of HIADs from Photogrammetric Wind Tunnel Data," AIAA Aerodynamic Decelerator Systems Conference, 25-28 March, 2013. AIAA 2013-1286. Daytona Beach, Fl.

[36] Johnson, Keith, Cassell, Alan, "HIAD 6m Inflatable Structure Static Load Test Report," NASA HIAD-IS-RP-11, April. 2012.

[37] Nyquist, Harry. "Certain factors affecting telegraph speed". Bell System Technical Journal, 3, 324–346, 1924

[38] Nyquist, Harry. "Certain topics in telegraph transmission theory", Trans. AIEE, vol. 47, pp. 617–644, Apr. 1928